Terahertz semiconductor laser chaos

Original
Terahertz semiconductor laser chaos / Liu, B.; Silvestri, C.; Zhou, K.; Ma, X.; Wu, S.; Li, Z.; Wan, W.; Zhang, Z.; Zhang, Y.; Peng, J.; Zeng, H.; Wang, C.; Brambilla, M.; Columbo, L. L.; Li, H.. - In: NATURE COMMUNICATIONS. - ISSN 2041-1723. - 16:1(2025). [10.1038/s41467-025-64921-x]

Publisher:
Nature

Published
DOI:10.1038/s41467-025-64921-x

nature communications

Article

https://doi.org/10.1038/s41467-025-64921-x

Terahertz semiconductor laser chaos

Received: 28 September 2024

Accepted: 25 September 2025

Binbin Liu[1,2,9], Carlo Silvestri[3,9], Kang Zhou[1,4,9], Xuhong Ma[1,4], Shumin Wu[1,2], Ziping Li[1], Wenjian Wan[1], Zhenzhen Zhang[1], Ying Zhang[5], Junsong Peng[5], Heping Zeng[4,5] ✉, Cheng Wang[6], Massimo Brambilla[7], Lorenzo Luigi Columbo[8] ✉ & Hua Li[1,2] ✉

In the terahertz (THz) range, due to the lack of effective THz light sources, chaos generation in THz semiconductor lasers, e.g., quantum cascade lasers (QCLs), is particularly challenging. Here, we experimentally demonstrate a THz chaos source based on a sole multimode THz QCL without any external perturbations. Such a dynamical regime is characterized by the largest Lyapunov exponent of the measured radio frequency signal of the laser. The experimental results are confirmed by our simulations based on effective semiconductor Maxwell-Bloch Equations. Furthermore, a reduced model based on two coupled complex Ginzburg-Landau equations is derived to systematically investigate the effects of the linewidth enhancement factor and group velocity dispersion on the chaotic regime. It is found that the chaos generation in the THz QCL is ascribed to the defect-mediated turbulence. Our findings pave the way for the generation of controllable and integrated THz chaos sources, as well as potential applications.

Chaos, characterized by aperiodic deterministic dynamics in nonlinear systems, has played a pivotal role in interpreting and controlling various ordered and disordered behaviors since its discovery[1]. In 1975, the principle of chaos generation in a laser system was first proposed[2]. Subsequently, the chaos phenomena were observed in several types of lasers, e.g., gas lasers[3], solid-state lasers[4], fiber lasers[5], and semiconductor lasers[6]. Chaos generation in lasers is relative to the type of laser. Lasers are typically classified into three classes-Class A, B, and C-based on the relations among the decay rates of the carriers, polarization, and photons[7–9]. Among the different kinds of lasers, semiconductor lasers serve as an ideal platform for the chaos investigation owing to its all-solid-state nature, on-chip integration, and rich nonlinearities. Most semiconductor lasers belong to Class B laser systems, being the carrier lifetime much longer than the photon lifetime[10]. Examples include quantum well lasers[11], quantum dot lasers[12], interband cascade lasers[6], and so on. Chaos generation in semiconductor lasers is typically constrained by system dimensionality and generally requires the introduction of external perturbations to occur[13], such as optical feedback[14], optical injection[15], optoelectronic feedback[16], loss modulation using a saturable absorber[17], etc. However, in particular cases, sufficiently strong nonlinear mode coupling between multiple longitudinal or transverse modes in semiconductor lasers can induce chaotic instabilities even without additional perturbations[9]. For example, chaos was observed in free-running vertical-cavity surface-emitting lasers without external perturbations, due to the nonlinear coupling between two elliptically polarized modes[8]. In addition, free-running quantum-dot micropillar lasers exhibited chaos when operated close to the quantum limit[12]. Moreover, transverse mode competition can cause filamentation, disrupting the stability of the frequency comb due to spatial hole burning (SHB) and the Risken-

---

[1]State Key Laboratory of Materials for Integrated Circuits and Key Laboratory of Terahertz Solid State Technology, Shanghai Institute of Microsystem and Information Technology, Chinese Academy of Sciences, Shanghai, China. [2]Center of Materials Science and Optoelectronics Engineering, University of Chinese Academy of Sciences, Beijing, China. [3]Institute of Photonics and Optical Science (IPOS), School of Physics, The University of Sydney, Camperdown, NSW, Australia. [4]Chongqing Key Laboratory of Precision Optics, Chongqing Institute of East China Normal University, Chongqing, China. [5]State Key Laboratory of Precision Spectroscopy, and Hainan Institute, East China Normal University, Shanghai, China. [6]School of Information Science and Technology, ShanghaiTech University, Shanghai, China. [7]Dipartimento Interateneo di Fisica, Politecnico di Bari e CNR-IFN (UOS Bari), Bari, Italy. [8]Dipartimento di Elettronica e Telecomunicazioni, Politecnico di Torino, Torino, Italy. [9]These authors contributed equally: Binbin Liu, Carlo Silvestri, Kang Zhou.
✉e-mail: hpzeng@phy.ecnu.edu.cn; lorenzo.columbo@polito.it; hua.li@mail.sim.ac.cn

Nummedal-Graham-Haken (RNGH) instability[18,19]. Additionally, transverse mode competition in microlasers can directly result in chaotic behavior[20].

Recently, extensive studies have been carried out on chaos phenomena in near-infrared semiconductor lasers, driven by their potential applications in high bit-rate optical communications[21], random number generations[22], light detection and ranging systems (LIDAR)[23–25], etc. However, in the terahertz (THz) frequency range, chaos generation in semiconductor lasers is challenging due to the scarcity of effective THz light sources and high-speed detectors. The THz chaotic behavior was experimentally observed in superconducting Josephson junctions[26] which required heavy cryogenic cooling down to 4.2 K and were not compatible with other III-V semiconductor devices. Additionally, a chaotic oscillating laser diode with optical delayed feedback was used to generate wide-range THz waves, which can be further employed for low-cost THz time domain systems[27,28]. Therefore, it is urgent to develop semiconductor laser-based THz chaotic sources for various applications as mentioned above. For instance, the THz chaotic LIDAR system can offer higher spatial resolution and greater resilience to interference[23]; Chaos-based broadband THz spectroscopy can be employed to investigate physical and chemical processes in biological and living systems, including transient biological structures, unstable molecules, and chemical reactions, which are challenging to observe using conventional spectroscopy tools[26].

The semiconductor-based quantum cascade laser (QCL)[29,30], which is generally categorized as a Class-A-like laser[31,32], is one of the most suitable sources for the chaos generation in mid-infrared and THz wavelengths. Unlike other THz sources that rely on femtosecond lasers or superconducting technologies, which often suffer from poor conversion efficiency and require bulky, complex equipment, electrically pumped THz QCLs combine a broad spectral tuning range, high output power, and pronounced nonlinear characteristics. These unique features not only enable the exploration and characterization of chaotic dynamics in the THz domain but also provide a cost-effective and practical alternative for advancing research in this field. In recent years, chaos generation in single-mode mid-infrared QCLs under optical feedback or injection conditions has been achieved[33,34]. However, the chaos dynamics in THz QCLs remain largely unexplored. It is worth noting that the gain recovery time in THz QCLs is longer than that in mid-infrared QCLs[35], and the carrier dynamics in THz and mid-infrared QCLs are different. Furthermore, QCLs exhibit a moderate but non-zero linewidth enhancement factor (LEF, or α factor), and when operated in a Fabry-Perot resonator configuration, the forward and backward propagating fields give rise to spatial hole burning (SHB) effects[36]. Both such effects contribute to the transition from single- to multimode emission in QCLs with low threshold in terms of laser pump. When the nonlinear effects cooperate with the group velocity dispersion (GVD), two operational regimes can be observed in free-running QCLs: one is the mode-locking or the frequency comb regime[32,37]; the other is the chaotic state.

Here, we demonstrate the chaos generation in a free-running multimode THz QCL emitting around 4.2 THz, without any external perturbations. The inter-mode beatnote (BN) of the THz QCL is measured and analysed while changing the bias current. Single narrow BN, multi-peak BN, and broad BN spanning over several GHz (chaotic state) are experimentally observed at different current pump conditions. Furthermore, the largest Lyapunov exponents calculated from the measured time traces of the broad inter-mode BN signals clearly prove the chaotic behavior. To further prove the chaos generation in the free-running THz QCL, a full model based on the Maxwell-Bloch equations and a reduced model based on two coupled complex Ginzburg-Landau equations are, respectively, employed to reproduce the experimental data and unveil the physical mechanism for the chaos generation in THz QCLs.

Results

Experimental setup and laser performance

Figure 1a shows the experimental setup employed for the chaos characterization for THz QCLs. As previously explained, the time and frequency characteristics of the laser are measured using the laser itself as a detector. A microstrip line, which is mounted close to the THz QCL chip, is used to achieve the impedance matching between the laser (or detector) and the external circuit for the transmission of high-frequency signals. A bias-T is used to provide the DC current to the THz QCL for lasing, and simultaneously, the AC port of the bias-T is used to extract the high-frequency components of the photocurrent signal. After the bias-T, the RF signal is amplified by 30 dB using a microwave amplifier. The inter-mode beatnote signals, which originate from the mixing of THz modes, are finally recorded using a spectrum analyser (frequency domain) and a high-speed oscilloscope (time domain) as shown in Fig. 1a. The inset of Fig. 1a shows an optical photo of the THz QCL mounted with a microstrip line and high-speed cable for high-frequency extractions. The THz QCL used in the experiment has a cavity length of 6 mm and a ridge width of 100 μm. The design and fabrication of the THz QCL are detailed in Methods.

Analyzing the chaos behavior primarily involves the time and frequency characteristics of a laser. For single-mode QCLs, a photodetector that can convert the optical signal to an electrical one is normally employed to characterize the time and frequency traces in the range from DC to hundreds MHz[6,33]. Note that in the lower frequency range around DC, the noise is usually large. Therefore, in this work, for the chaos in multimode THz QCLs, we can alternatively measure the RF signal around the inter-mode BN frequency of the laser rather than the signal around DC. In principle, the frequency and time characteristics around the fundamental inter-mode BN are identical to those measured around DC. But, the cleaner signal can be obtained when we perform the measurement at higher frequencies around the inter-mode BN due to the lower noise. Moreover, to detect the inter-mode BN signal of the laser, the laser self-detection scheme is employed[38,39]. Due to the fast carrier relaxation time in THz QCLs, the QCL itself can be used as a fast mixer to detect the beating of the longitudinal modes in the QCL cavity. The beating of the modes will bring about the modulation of population inversion, which is then converted into current modulation. The current modulation can finally be measured directly from the laser and displayed on a spectrum analyzer or a fast oscilloscope.

Figure 1b demonstrates the light-current-voltage (*L*–*I*–*V*) characteristics of the THz QCL measured in continuous wave (CW) mode at a heat sink temperature of 15 K. The laser shows a maximum output power of 0.9 mW and a threshold current of 470 mA at 15 K. Note that the power shown here is the collected power without considering any calibrations for water absorption, window transmission, light collection efficiency, and so on. The emission spectra of the QCL measured using a Fourier transform infrared (FTIR) spectrometer is shown in Fig. S1, Supplementary Information. Figure 1c shows the inter-mode BN map as a function of bias current measured when the laser is operated in free-running. Three current regions, labeled as narrow BN, multi-peak BN, and broad BN, can be clearly observed. When pumped at lower currents between 525 and 620 mA, single-peak narrow BNs at 6.08 GHz are obtained, indicating the frequency comb operation. From 620 to 690 mA, we can see a clear change in the inter-mode BN signal from single peak to multi-peak behavior. As the current grows beyond 690 mA, the inter-mode BN signal is characterized by a broad bandwidth spanning over 1 GHz (measured at the noise floor). It is worth noting that broad inter-mode BN signals spanning over 1 GHz (measured at the noise floor) have already been experimentally observed[38,40,41]. However, the presence of broad inter-mode BN is not proof of chaos generation; rather, it merely indicates the unlocking of laser modes. Analyzing methods such as phase portraits, Lyapunov

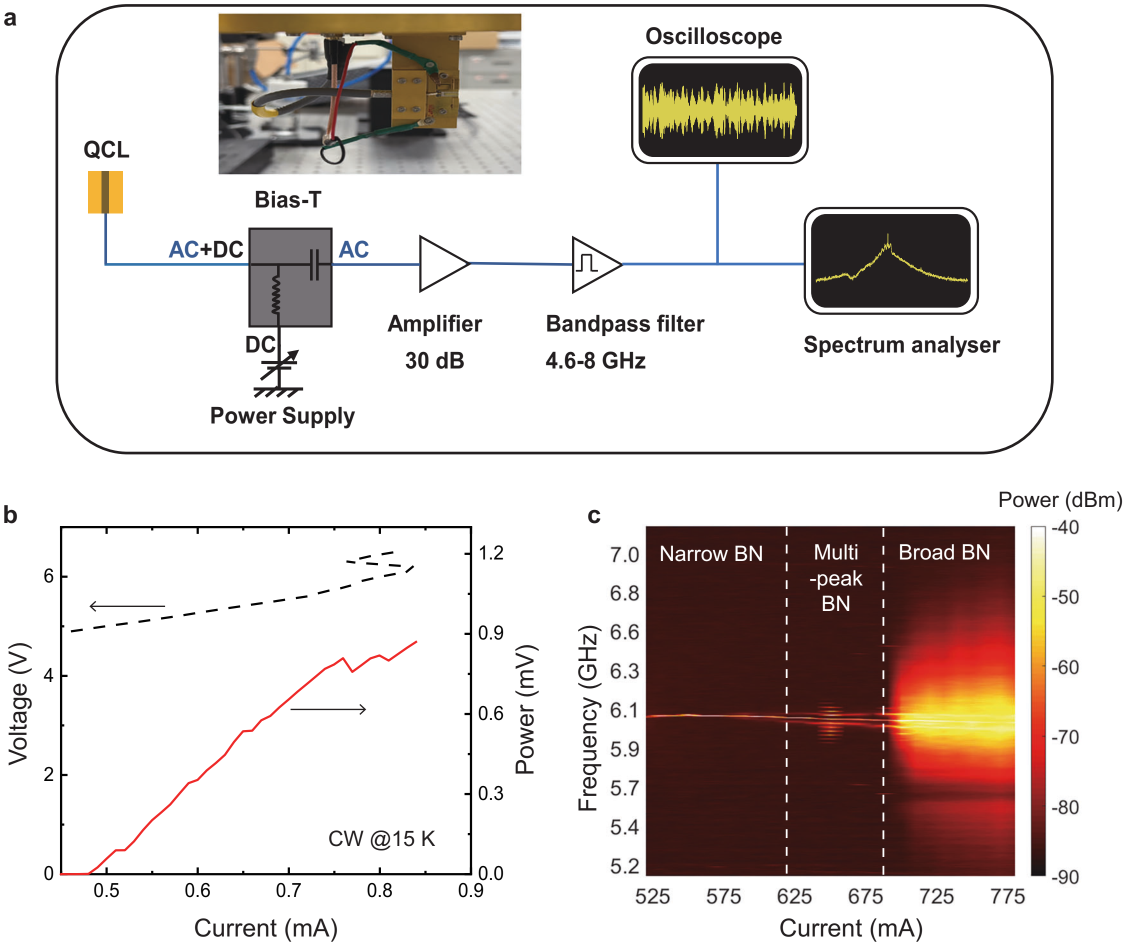

Fig. 1 | Experimental setup and laser performances. a Experimental setup employed for chaos characterizations of THz QCLs. The laser self-detection scheme is used for the measurement of inter-mode beatnote signals, which are finally recorded in frequency and time domains using a spectrum analyzer and a high-speed oscilloscope (20 GS/s), respectively. To extract cleaner inter-mode beatnote signals, a microwave amplifier with a gain of 30 dB and a bandpass filter (4.6–8 GHz) are used. **b** Light-current-voltage characteristics of the QCL measured in cw mode at 15 K. **c** inter-mode beatnote maps of the QCL, measured with a resolution bandwidth of 10 kHz and video bandwidth of 1 kHz. The current step is 10 mA. The vertical dashed lines identify three current intervals corresponding to different operating regimes.

spectra, and correlation dimension are essential for demonstrating chaos generation.

Chaos measurement and analysis

In Fig. 2a, b, we show the recorded frequency spectra and corresponding time traces of the inter-mode BN signals, respectively, measured at different bias currents. As the current is raised from 540 to 760 mA (from top to bottom panel in Fig. 2a), inter-mode BN spectra, recorded with a resolution bandwidth (RBW) of 10 kHz and a video bandwidth (VBW) of 1 kHz, show clear transitions from a single narrow peak (frequency comb), multi-peak, to a broad peak. The corresponding time traces of the signal are shown in Fig. 2b for a time duration of 500 ns. At 540 mA, as shown in the top panel of Fig. 2b, the time trace exhibits a sinusoidal periodic time series. As the current is increased to 650 mA, a modulation on the sinusoidal time trace is clearly observed, which corresponds to the multi-peak inter-mode BN. When we further increase the current to 700 or 760 mA, typical chaotic time traces without any accurate and predictable periodicity are observed, showing the laser enters the chaotic regime. Additionally, the frequency and temporal characteristics of BN at more current values are shown in Figs. S2 and S3, Supplementary Information. Note that even in the chaotic regime, the fundamental oscillations around inter-mode BN frequencies can always be observed. These fundamental oscillations exist in all time traces measured at different currents, see Fig. S4 in Supplementary Information.

The phase portrait of a time series can be constructed by applying a time lag on the original time series[42]. For example, here single time step (τ) employed in the time trace measurements is used as the time lag. In Fig. 2c, four phase portraits calculated from time traces shown in Fig. 2b at different currents are plotted. A periodic system normally shows an inner circle in its two-dimensional phase portrait, as shown in the first panel of Fig. 2c for 540 mA. At 650 mA, the phase portrait becomes irregular, and the inner circle disappears. The phase portraits become more complex at higher currents, e.g., 700 and 760 mA, and much stronger oscillations result in larger trajectories in phase portraits. Furthermore, Supplementary Movie 1 visually shows the trajectories for the four different cases mentioned above. At 540 mA, it can be clearly seen that a regular winding around the origin is obtained, which indicates a period-one orbit (comb operation). As the current is increased, the system demonstrates a more complex behavior, i.e., the trajectory is firstly refined in an inner zone loop, followed by an eccentric shift toward the outer region. Note that at 650 mA, although the trajectory is much more complex than that obtained at 540 mA, a repeated amplitude-time trace can be observed, which refers to a quasi-periodic oscillation. The irregular traces observed at 700 and 760 mA suggest that the system enters a chaotic state, as the following characterization of Lyapunov exponent and correlation dimensions

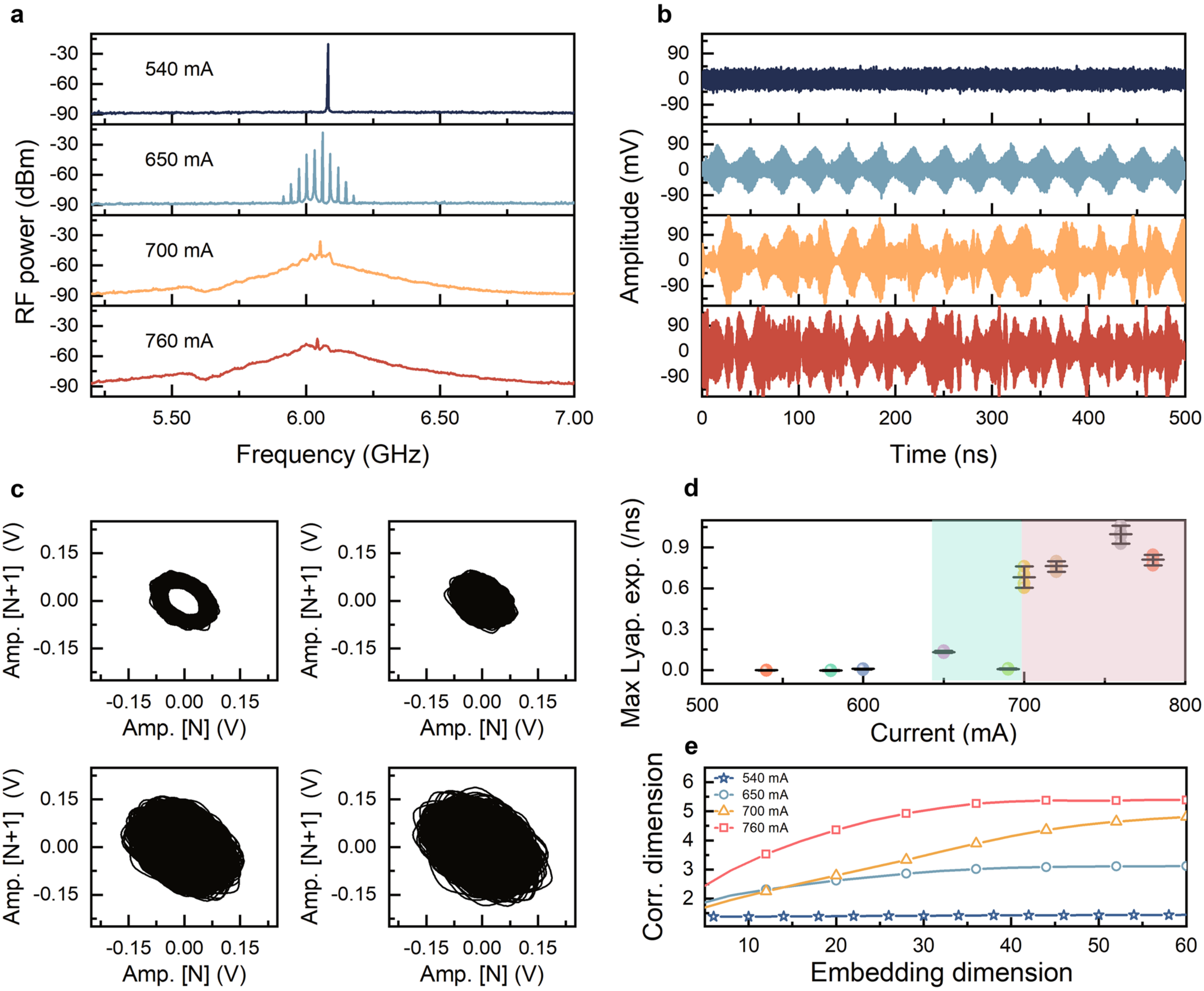

Fig. 2 | Experimental results. a, **b** Electrical spectra and corresponding time traces measured at different currents. The electrical spectra were recorded with a resolution bandwidth of 10 kHz and a video bandwidth of 1 kHz. In (**a**) and (**b**), from top and bottom panels, the current is increased from 540 to 760 mA. **c** Phase portraits at various currents obtained from time trace with a time length of 500 ns. **d** Calculated maximum Lyapunov exponents. The shaded pink region corresponds to the chaotic regime, and the shaded green region represents the transition region from comb to chaos. We measured 5 times at each current, which gives the error bars in the figure. **e** Correlation dimension versus embedding dimension for the four different currents.

will demonstrate the chaos generation. We also re-plot the trajectories by reducing the data sampling rate, e.g., data were collected for every 1500τ. The results summarized in Supplementary Movie 2 show that at 540 mA the trajectory almost converges to a single point indicating a perfect periodic oscillation (comb state). Similar expansion of the trajectories with current is also observed in Supplementary Movie 2.

We offer a specific proof of chaos in our QCL emission by evaluating the Lyapunov exponents of the recorded series. We extract the largest Lyapunov exponent as shown in Fig. 2d by using Wolf's algorithm[43]. Calculating the largest Lyapunov exponents has always been a powerful tool to identify chaos, reflecting the average exponential rate of divergence for nearby orbits in the phase space. In a stable system, the exponents are negative; while in a chaotic system, at least one positive Lyapunov exponent exists. From Fig. 2d, we can see that as the current is below 600 mA, the largest Lyapunov exponents are negative values, which indicate stability with narrow inter-mode BN signals. When the QCL presents multi-peak BNs between 600 and 700 mA, the largest Lyapunov exponents become positive but smaller than 0.15/ns, which shows the transition region from comb to chaos. As broad inter-mode BNs appear (>700 mA), the calculated max Lyapunov exponents become much larger, and especially it reaches 1/ns at 760 mA as shown in the shaded area in Fig. 2d, which indicates the system enters the chaotic regime. To ensure reliability, we conducted five measurements of the time traces for each current depicted in Fig. 2b, and corresponding Lyapunov exponents with error bars are shown in Fig. 2d. We also investigated the impact of the sampling rate on the Lyapunov exponent, employing two sampling rates of 20 and 40 GS/s to acquire the time-domain signals. Figure S7a (Supplementary Information) illustrates the calculated Lyapunov exponents for different drive currents (i.e., 540, 650, and 760 mA). For each current and sampling rate, five measurements were carried out. The results reveal that the Lyapunov exponents exhibit no significant dependence on the time resolution. Additionally, Fig. S7b (Supplementary Information) presents the corresponding 500-ns time traces measured at 760 mA for two different sampling rates.

To further investigate the chaotic properties and system complexity, we calculated the correlation dimensions of different states using the Grassberger-Procaccia (GP) algorithm[44,45]. This algorithm computes the correlation dimension by plotting the correlation integral $C(r)$ as a function of the sphere radius r for varying embedding

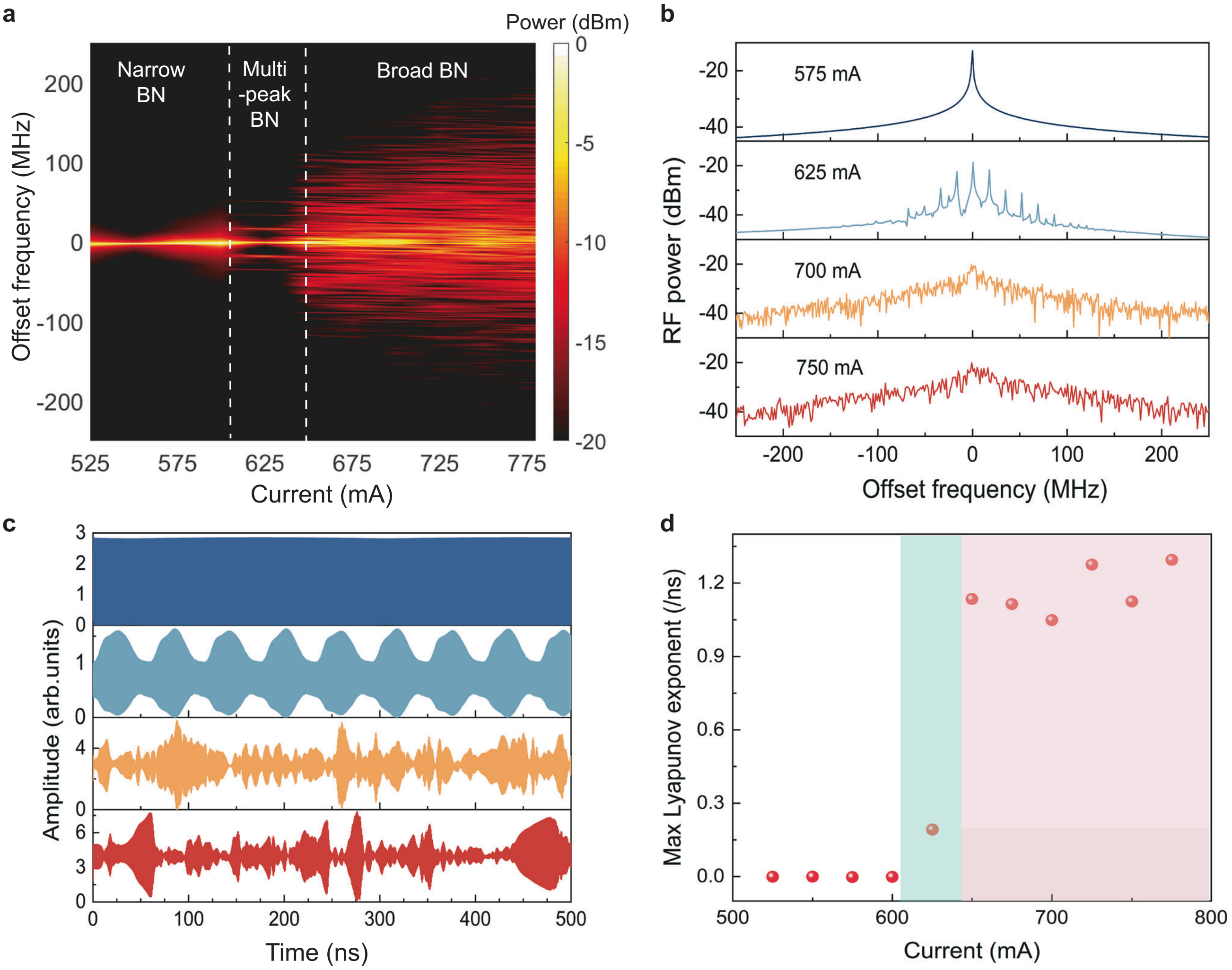

Fig. 3 | Simulated results obtained from the full model. a inter-mode beatnote map of the THz QCL. The current step is 25 mA. The vertical dashed lines identify three distinct regimes, i.e., single narrow beatnote, multi-peak beatnote, and broad beatnote. **b**, **c** Simulated electrical spectra and corresponding time traces for four different bias currents. In (**a**) and (**b**), the frequencies have been offset by the center frequency of the inter-mode beatnote signal. In (**b**) and (**c**), the drive current is increased from 575 to 750 mA from top to bottom panel. **d** Calculated largest Lyapunov exponents.

dimensions (m). It serves as a tool to distinguish between noise and chaos: chaos exhibits a correlation dimension that saturates with increasing m, whereas noise does not. As shown in Fig. 2e, it is clearly shown that the states at 700 and 760 mA are indeed in chaotic situations because the saturated correlation dimensions are obtained. Detailed results of the GP algorithm for these dynamic states are provided in Fig. S5 (Supplementary Information). At a pump current of 760 mA, the signal exhibits the highest correlation dimension, approximately 5. However, the Lyapunov spectra reveal only one positive Lyapunov exponent greater than zero (see Fig. S6, Supplementary Information), indicating that the chaotic system is not hyperchaotic, as hyper-chaos requires at least two positive Lyapunov exponents. We experimentally quantify the chaos bandwidth of the THz laser, and its comparison with other lasers is summarized in Table S3 (Supplementary Information). Note that the effective bandwidth of the broadband chaotic signals was determined by summing the discrete spectral segments of the chaos power spectrum that collectively account for 80% of the total power. Using this approach, a chaotic signal bandwidth of 180 MHz is obtained. It can be seen from Table S3 (Supplementary Information) that the QCL chaos bandwidths are far smaller than those measured from near-infrared lasers. However, the chaos bandwidth measured in this work is comparable to those reported for mid-infrared QCL chaos sources.

Simulation model and results

We provide here sets of simulations to validate the chaotic characteristics of the QCL emission as observed in the experiment, as shown in Fig. 2. The effective semiconductor Maxwell-Bloch equations (ESMBEs) have been adopted to investigate the nonlinear dynamics in semiconductor lasers[46], and specifically QCLs[47–49]. In this work, we thus presently adapt this model to the Fabry-Perot (FP) laser configuration to study the chaotic behavior in THz QCLs, tailoring it to the characteristics of the device studied in the experiments, adopting the parameter set in Table S1, provided in the Supplementary Information. Figure 3a displays the simulated inter-mode BN map of the THz QCL. We observe that the sequence of regimes observed in Fig. 1c (single narrow BN, multi-peak BN, and broad BN) is reproduced with remarkable agreement in the simulations, although we note a slight discrepancy in the bias current values at which they occur. This is likely due to some additional dissipative effects or efficiency issues in the real device, which are not encompassed by the model.

Figure 3b shows four sections of the inter-mode BN map (Fig. 3a) obtained at 575, 625, 700, and 750 mA (from top to bottom panels). Note that to avoid the influence of higher harmonic frequency components on the time traces, and thus enable a direct comparison with the experimental traces (Fig. 2b), a digital filtering method is implemented. The filtered simulated time traces are shown in Fig. 3c, while the original traces without filtering are shown in Fig. S8 (Supplementary Information) for reference. We highlight that the traces in Fig. 3c represent the filtered output power retrieved from the ESMBE model, which can be compared with the voltage traces in Fig. 2b, given the proportionality between these two quantities[50,51]. Similar to Fig. 2b, the simulated traces show clear evolution from a pure sinusoidal oscillation at 575 mA, to a modulated sinusoidal time trace at 625 mA and finally reach the chaotic regime beyond 700 mA. To see the detailed structure of the time traces, we show the zoom-in of Fig. 3c in a time scale of 20 ns in Fig. S9 (Supplementary Information).

Consistent with what was done for the experimental traces, the Lyapunov exponents have also been computed for the simulated regimes. In Fig. 3d, the calculated largest Lyapunov exponents are plotted as a function of the bias current for the simulated traces. We observe the same transition to the chaotic regime as that observed in the experiment (see Fig. 2d). This is excellent evidence of the concordance between the experiment and the model. In detail, we find that below 600 mA, the largest Lyapunov exponents are negative, an indication of regular laser dynamics. As the current is increased to 625 mA, an intermediate regime (green band) with exponents around 0.17/ns is observed. Beyond 650 mA, the values of the Lyapunov exponents range between 0.9 and 1.3/ns (see the shaded pink region in Fig. 3d). This region is therefore characterized by chaotic dynamics, with Lyapunov exponent values of the same order of magnitude as those calculated for the experimental traces in the chaotic region (see the shaded area in Fig. 2d). For the simulated results, we also investigated the impact of the sampling rate on the Lyapunov exponent. 7 sampling rates of 18, 20, 22, 24, 26, 30, and 40 GS/s were employed to acquire the time-domain signals. The corresponding Lyapunov exponents for different drive currents are presented in Fig. S10 (Supplementary Information). Similar to the findings in Fig. S7 (Supplementary Information), the Lyapunov exponents exhibit no significant dependence on the time resolution. To summarize, the simulations based on the full model clearly demonstrate a strong agreement with the experimental findings. This agreement is evident both in the dynamic scenario, as the bias current varies, where we observe the onset of chaos transitioning through narrow BN and multi-peak BN regimes, and in the similarity between the experimental and simulated time traces and RF spectra. Furthermore, there is also consistency between simulation and experiment regarding the order of magnitude of the Lyapunov exponents within the chaotic region.

Since the simulated sequences effectively replicate the experimental ones, this reassures us about the transition to the chaotic regime, characterized by a shift from narrow to broad linewidths. In principle, when the laser enters a chaotic state, the frequency fluctuations increase dramatically, resulting in a significant broadening of the spectral linewidth, which is caused by the collapse of coherence[10,15,52]. However, experimentally characterizing the linewidth of optical modes in the THz frequency range poses challenges due to the limited spectral resolution of THz spectrometers (see the optical spectra of the THz QCL in Fig. S1, Supplementary Information). Here, we analyze the optical lines in the simulated traces to determine if optical chaos is indeed present. In the left column of Fig. 4, the simulated optical spectra at three bias current values corresponding to three different dynamical regimes are shown: 575 mA (comb operation with a single narrow BN), 625 mA (multi-peak BN), and 750 mA (broad BN). In the right column, a zoom of a single optical line from the corresponding spectrum shown in the left column is displayed. We observe that at 575 mA, the single optical line of the frequency comb exhibits a narrow linewidth (Fig. 4a). Increasing the current to 625 mA (Fig. 4b), the zoomed-in view of the single optical line reveals multiple peaks, which result in the multi-peak feature in the inter-mode BN (see Figs. 2a and 3b). As the current is increased to 750 mA, where the max Lyapunov exponent is large and positive, flagging chaotic regime, it can be seen that the optical spectrum is significantly broadened and simultaneously each optical line also demonstrates broad linewidth which spans over 200 MHz (Fig. 4c). The chaos characterized by positive Lyapunov exponent in regimes of broad BN in the RF range can thus be ascribed to a multimode chaotic dynamics.

To gain deeper insights into the physical mechanisms behind chaos generation in THz QCLs, we developed a reduced model, based on the formerly described full ESMBE model, which under appropriate approximations such as the near-threshold operation, can be reduced to a pair of coupled complex Ginzburg-Landau equations (CGLEs)[53]:

$$\frac{\partial F^+}{\partial \eta} + \frac{\partial F^+}{\partial t} = -F^+ + (1+i\alpha)\mu F^+ - (1+i\alpha)^2(|F^+|^2 + 2|F^-|^2)F^+ + \left(\frac{\sigma^2}{\Gamma^2(1+i\alpha)} + i\frac{\upsilon_g}{2\tau_p}k''\right)\frac{\partial^2 F^+}{\partial \eta^2} \tag{1}$$

$$-\frac{\partial F^-}{\partial \eta} + \frac{\partial F^-}{\partial t} = -F^- + (1+i\alpha)\mu F^- - (1+i\alpha)^2(|F^-|^2 + 2|F^+|^2)F^- + \left(\frac{\sigma^2}{\Gamma^2(1+i\alpha)} + i\frac{\upsilon_g}{2\tau_p}k''\right)\frac{\partial^2 F^-}{\partial \eta^2} \tag{2}$$

where F^+ and F^- are respectively the scaled forward and backward electric field envelopes, α is the linewidth enhancement factor, μ is the scaled pump parameter, σ is the ratio between polarization dephasing time τ_d and photon lifetime τ_p, Γ is the scaled gain bandwidth of the QCL medium, η and t are the scaled spatial and temporal coordinates, υ_g is the group velocity, and k'' is the waveguide GVD.

The reduced mathematical complexity of this model compared to the full ESMBEs, along with its ability to describe QCL dynamics in terms of a universal class of equations like the CGLEs, makes it better suited for obtaining insights into the origin of physical phenomena, such as the formation of chaos in our case. A description of the reduced model can be found in the section Methods. For further details, see ref. 53. We firstly exploit the reduced model to perform emission characterization at different values of the normalized pump parameter p, defined as the ratio between μ and its threshold value (μ_{th}), i.e., $p = \frac{\mu}{\mu_{\text{th}}}$. Also in this case, we adopt parameter values consistent with our experimental device (see Table S2 in the Supplementary information). As p increases, we observe a transition from single-mode emission ($p = 1.01$) to a frequency comb ($p = 1.9$), and finally to chaotic dynamics at $p = 3.15$, which is shown in Fig. S11 (Supplementary Information). The chaotic nature of this regime is rigorously assessed by calculating the Lyapunov exponent value, which is 1.16/ns. Additionally, in line with expectations, the other two regimes exhibit negative Lyapunov exponents, namely -9.5×10^{-4}/ns and -4.29×10^{-3}/ns, in agreement with the experimental results of Fig. 1c, b, and S1 (Supplementary Information). However, we observe a slight discrepancy in the pump value associated with chaotic dynamics compared to both the experiment and the full model simulations. We attribute this difference to the approximations implemented for the derivation of the reduced model, particularly the assumption of near-threshold operation[53].

Having verified that the reduced model correctly reproduces the transition between dynamic regimes reported in the experiment as the pump varies, we can employ it for a more in-depth analysis of the effect of certain physical parameters on the formation of chaos. Among all the physical parameters of QCLs, it has been highlighted in the literature that non-zero α factor and GVD have a significant impact on the

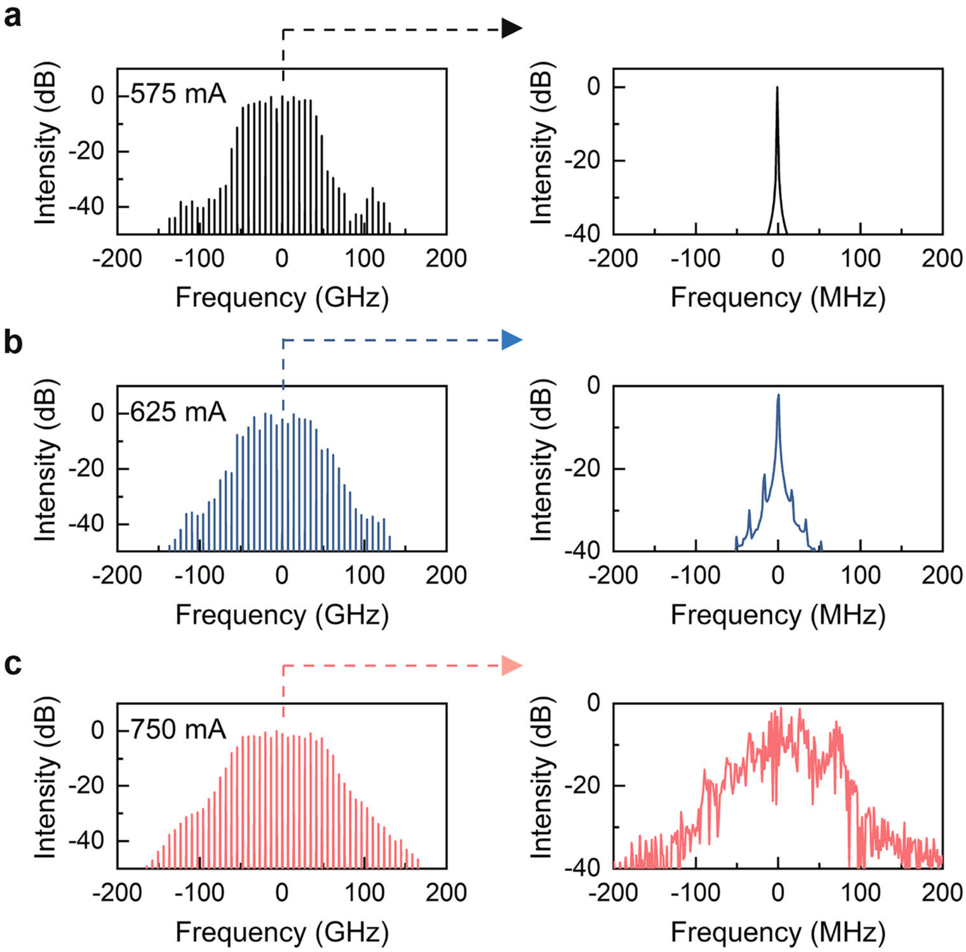

Fig. 4 | Simulated optical spectra and the linewidth analysis. Left column: Optical spectra at 575 (**a**), 625 (**b**), 750 mA (**c**). Right column: zoom around one peak of the optical spectrum in the left column. For each spectrum, the intensity values are normalized with respect to the maximum.

multimode dynamics of QCLs, particularly on the formation of frequency combs[32,36,54,55]. Here, we examine the role played by these two parameters in the formation of multimode chaos in these devices.

We first investigate the impact of the α factor on the temporal and spectral characteristics of THz QCL emission. To assess its effect, we vary α while keeping the values of the other parameters fixed. In addition to the parameter values provided in Table S2, we specify that the pump is set to p = 1.9, while the GVD consists of the intrinsic material contribution, $\mathrm{GVD_{mat}} = -77024\ \mathrm{fs^{2/mm}}$. The waveguide GVD, denoted as k'', which is included as a phenomenological parameter in the model and can be varied, is set to zero. Details on the estimation of $\mathrm{GVD_{mat}}$ and the incorporation of k'' into the model, which follows the approach used in ref. 18, are provided in Methods. The values of α used in this study are consistent with experimental measurements reported in the literature for this parameter in QCLs[36,54,56]. The results are depicted in Fig. 5a–c. We note that an increase in α from 0.9 to 1.15 results in the destabilization of the single mode emission of Fig. 5a in favor of a multimode state, in this case a frequency comb (Fig. 5b). This is in line with expectations, as the increase in α corresponds to an increase in the coupling between phase and amplitude of the field, identified as one of the mechanisms responsible for the destabilization of CW emission in QCLs[47,55]. A further increase in α to 1.4 leads to the emergence of an unlocked multimode state characterized by erratic behavior of the output power, and broadening of optical spectrum and fundamental inter-mode BN (Fig. 5c). As presented in the table of Fig. 5f, the calculated Lyapunov exponent value of 1.12/ns for this regime confirms its chaotic nature, in contrast to the negative values found for the CW and comb states of Fig. 5a, b. We note that the observed positive value of the Lyapunov exponent is very close to those reported for chaotic states in experiments and simulations with the full model (see Figs. 2d and 3d). Furthermore, we highlight that theoretical studies have shown that an increase in the α factor, and thus in phase-amplitude coupling, leads to the emergence of irregularities in the dynamics of QCLs[32,48], resulting in a loss of locking, identified by the broadening of the fundamental inter-mode BN in the RF spectrum. Here, through the calculation of the Lyapunov exponents, we demonstrate how this corresponds to the onset of chaos. Therefore, higher values of α favor the formation of chaos in free-running THz QCLs.

In addition to the α factor, we investigate the role of the GVD for chaos generation. Regarding comb operation in QCLs, the crucial role of the GVD is well known, since it has been shown that it regulates the field phase dynamics, contributing to establish a regime of chirped instantaneous frequency and thus determining the modulation frequency behavior of QCL combs[32]. Furthermore, the GVD required for the comb operation depends on the α factor value. This implies that the range of GVD values where unlocked dynamics are observed features a dependence on α factor[32]. In our study, we fix α = 1.15 and investigate the formation of chaos as the GVD varies. The contribution of the QCL material, $\mathrm{GVD_{mat}}$, is fixed to $-77024\ \mathrm{fs^2/mm}$, while we tune k'' by setting it to −15,000, 0, and 15,000 $\mathrm{fs^2/mm}$. Consequently, the total GVD ranges from −92,024 $\mathrm{fs^2/mm}$ to −62,024 $\mathrm{fs^2/mm}$, values compatible with experimental measurements of this parameter for THz QCLs[57]. In Fig. 5d, b, e, we

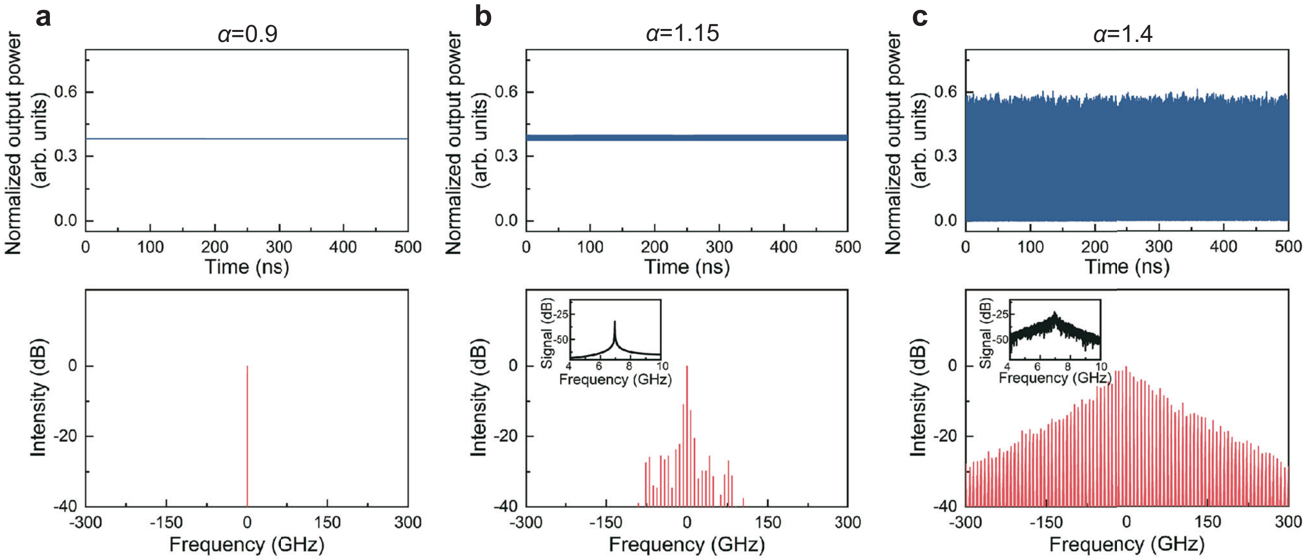

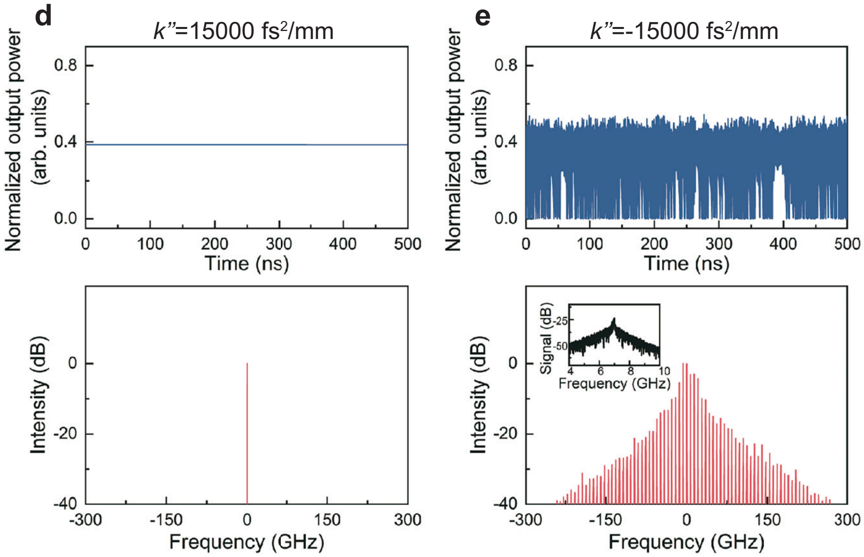

f

α factor	k” (fs²/mm)	Max Lyapunov exponent (/ns)
0.9	0	-4.30×10^{-3}
1.15	0	-4.29×10^{-3}
1.4	0	1.12
1.15	15000	-4.07×10^{-3}
1.15	-15000	0.98

Fig. 5 | Effects of *α* factor and group velocity dispersion on the time and spectral characteristics of the THz QCL. a–c Scan of *α* factor from 0.9 to 1.4. The upper panels display the time traces by varying *α* factor, and the corresponding optical spectra are shown in the lower panels. The insets in (**b**) and (**c**) are inter-mode BN spectra. For these simulations, the pump parameter is set to $p = 1.9$, and the waveguide group velocity dispersion is set to $k'' = 0$. **d**, **e** Scan of k''. The upper panels show the time traces by varying k'' from -15,000 to 15,000 fs²/mm, and the corresponding optical spectra are shown in the lower panels. The inset in (**e**) is the inter-mode BN spectrum. For these simulations, $p = 1.9$ and $\alpha = 1.15$. **f** Calculated largest Lyapunov exponents.

show the simulated optical spectra and time traces obtained with the reduced model for k''=15,000 fs²/mm, 0, and −15,000 fs²/mm, respectively. The pump value is $p = 1.9$ and the other parameters are as in Table S2. We observe a CW-comb-chaos sequence as the GVD decreases, similar to what we observed with increasing *α* in Fig. 5a–c. We remark that the chaotic nature of the regime in Fig. 5e has been assessed by evaluating the maximum Lyapunov exponent, which exhibits a positive value of 0.98/ns (see Fig. 5f). Various experimental methods, such as chirped mirrors[58], Gires-Tournois interferometer (GTI) mirrors[59–61], and coupled cavities[62], have been employed to tune the GVD in QCLs, primarily with the intent of enhancing frequency comb stability. Our results suggest that these techniques could also be used to enhance chaos operation in these devices. Furthermore, we note that the observed transition from comb to chaos as the GVD decreases aligns with previous studies, which showed that below a certain GVD threshold, the QCL multimode dynamics become unlocked due to a significant reduction in the slope of the inter-mode phase spectrum[32].

In order to investigate the impact of some parameters on the chaos properties, we conducted additional simulations based on the full model ESMBEs. Firstly, we analyzed the Maximum Lyapunov Exponent as a function of the laser's drive current for each *α* value (*α* = 0.4, 0.7, and 1), as shown in Fig. S12a (Supplementary Information). As *α* increases, chaotic regimes expand, with all states becoming chaotic for *α*= 0.7 and 1. This indicates that higher *α* values enable chaotic behavior closer to the threshold. Moreover, we studied the effect of gain bandwidth on chaos in THz QCLs (Fig. S12b, Supplementary Information). For bandwidths above 0.5 THz, all states become chaotic. A bandwidth of 1.25 THz increases the Lyapunov exponents by 50% in the 700–750 mA range compared to the 0.5 THz case. This suggests that chaotic emission in QCLs can be enhanced by using devices with a large gain bandwidth, such as those based on multiple-stack active regions, which can achieve values above 1 THz[38,40]. Therefore, utilizing a high-gain bandwidth not only expands the chaotic current range but also significantly increases the Lyapunov exponent values, which could contribute to the hyper-chaos generation, meeting the requirements

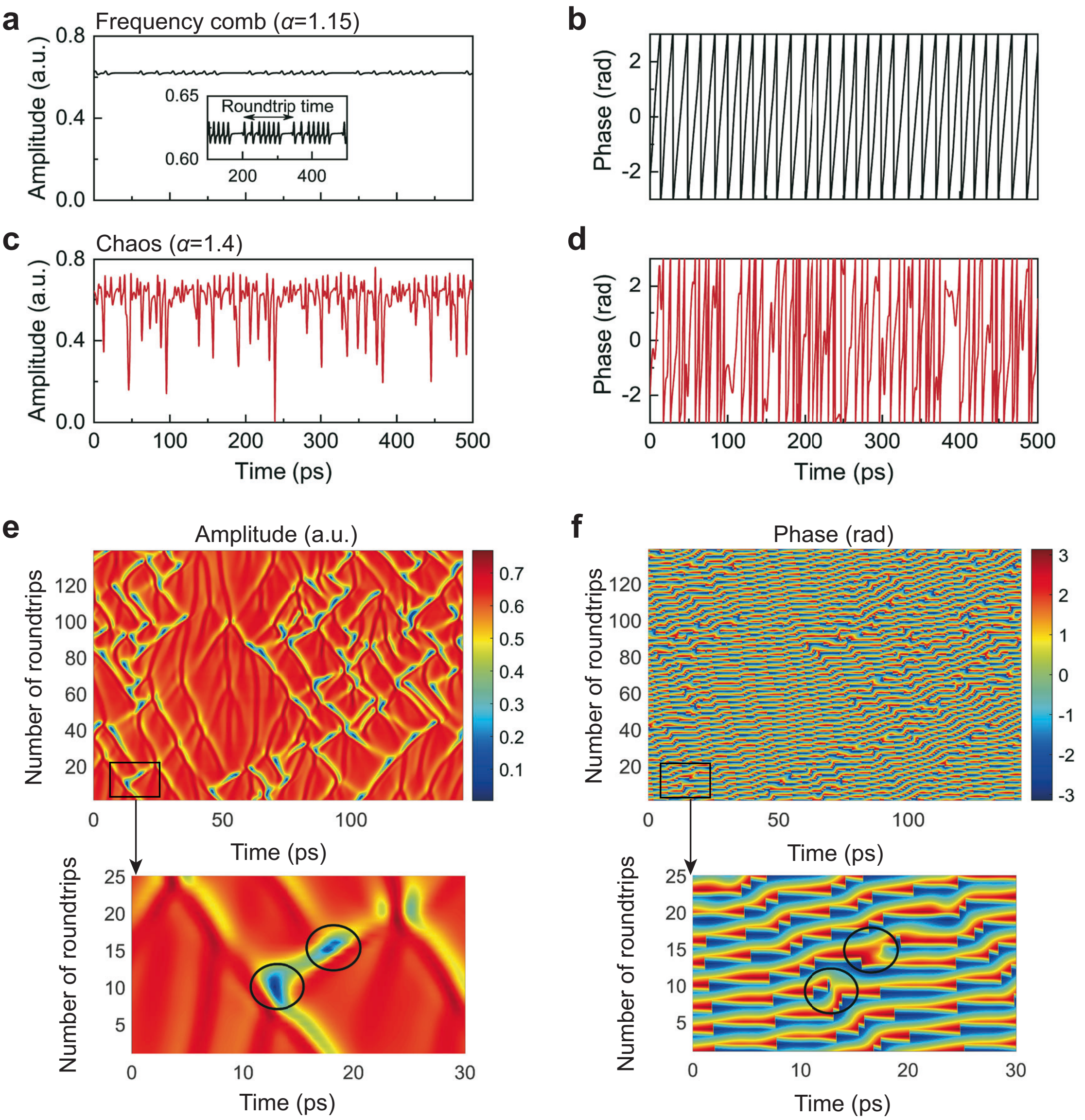

Fig. 6 | Field amplitude and phase for the multimode THz QCL chaos. Simulated amplitude and phase of the output field as a function of time for frequency comb (**a**, **b**), and multimode chaos regime (**c**, **d**) of the THz QCL. For the frequency comb regime α=1.15, while for the chaotic state $\alpha = 1.4$. For both regimes p=1.9 and k''=0, and other parameters as in Table S2. The inset in (**a**) shows a zoom of the amplitude trace. 2D map for amplitude (**e**) and phase (**f**) of the chaotic regime of (**c**, **d**) with time related to a roundtrip on the x-axis, and the number of roundtrips on the y-axis. The zoomed-in areas highlighted with a black rectangle are shown in the bottom panels, where defects in the field amplitude and the corresponding dislocations in the phase are circled in black.

of advanced applications that rely on robust and complex chaotic signals.

At this point we further employ the reduced model to gain insight into the physical origin of chaos in QCLs. Figure 6a–d show amplitude and phase of the output field as a function of time for the simulated regimes depicted in Fig. 5b, c, corresponding to two different values of α. In particular, Fig. 6a, b are related to the comb emission presented in Fig. 5b, while Fig. 6c, d represent the chaotic state of Fig. 5c. We observe that for the comb state, the amplitude trace exhibits a regular repetition of shallow structures with a period given by the cavity roundtrip, superimposed on a constant background. Additionally, the phase spans the entire interval from $-\pi$ to π, with a regular repetition of sawtooth-like structures. It is interesting to note how this corresponds to the regime of frequency combs induced by phase turbulence associated with the formation of homoclons[63] as recently reported in unidirectional ring QCLs[55,64] and not yet experimentally observed in the FP configuration. In contrast, the chaotic state (see Fig. 6c, d) exhibits the coexistence of erratic behavior for both amplitude and phase, the former with random oscillations between 0 (field defects) and a maximum value, and the latter presenting irregular dynamics while spanning the interval from $-\pi$ to π. These features correspond to the so-called defect-mediated turbulence (DMT) regime, which is well-known as a dynamic behavior for CGLE systems[63].

To better characterize this regime, we collected 20 ns time traces of the field phase and amplitude and after dividing each of them in segments of duration equal to the cavity roundtrip time we stacked these segments on top of each other obtaining a spatio-temporal representation of the 1D system dynamics shown in Fig. 6e, f; on the horizontal axis it is reported the fast temporal scale associated with the system evolution during a single roundtrip, while the vertical axis shows its evolution over a much slower temporal scale measured in units of roundtrips. In the amplitude map, multiple points of zero intensity (defects), depicted in dark blue, can be identified and, as previously mentioned, are characteristic of the DMT regime. A zoomed-in view of a region containing two defects is shown in the bottom panel of Fig. 6e, with the defects circled. The bottom panel of Fig. 6f shows the corresponding region in the phase map, where dislocations (also circled) align with the defect positions in the amplitude map as expected (see e.g. Fig. 5 in ref. 65 and Fig. 8 in ref. 63). Therefore, having reduced the dynamics of QCLs to a system of two coupled CGLEs, reproducing DMT states with parameters compatible with the experimental device, and the fact that the values of the Lyapunov exponents calculated for these DMT states are very close to those calculated for the chaotic experimental traces, suggest that the origin of chaos in THz QCLs can be attributed to the DMT.

Discussion

In summary, we have demonstrated chaos generation and its characterizations in free-running THz QCLs. Experimentally, by varying the bias current, the inter-mode BN signal showed clear transitions from single narrow BNs around the laser threshold to multi-peak BNs, and further into a chaotic regime characterized by broad BNs, spanning several GHz at high bias currents. The calculated largest Lyapunov exponents from the experimental time traces exhibited positive values at high currents, indicating chaos generation. In contrast to chaos generation in single-mode mid-infrared lasers, which typically requires external perturbations, we demonstrate THz chaos in free-running THz QCLs by leveraging their intrinsic multimode dynamics. Firstly, our laser operates in the THz wavelength range, which offers distinct advantages over the mid-infrared band. The THz frequency band is considered a promising candidate for ultra-broadband applications in next-generation communication systems, bridging the gap between millimeter waves and optical frequencies. Particularly for indoor applications, the THz band facilitates easier beam tracking and can utilize reflection paths to enhance link gains, providing significant advantages for mobile and indoor communication systems. Secondly, our work demonstrates the direct generation of chaos in free-running THz QCLs simply by adjusting the drive current, eliminating the need for external perturbations. In systems with external optical feedback, the chaotic bandwidth is strongly influenced by the feedback ratio[66,67] as well as the laser intrinsic properties. While in our approach, the chaos bandwidth is only governed by the intrinsic properties of the laser, e.g., α factor, GVD, gain bandwidth, etc. Finally, it is worth noting that in our THz QCL system, we demonstrate that modulation of the drive current enables dynamic and seamless transitions among distinct operational regimes, e.g., single-mode operation, frequency comb generation, and multimode chaotic emission, all within a single device architecture. This not only provides an ideal platform for investigating fundamental nonlinear dynamics in semiconductor lasers but also offers unprecedented flexibility in mode selection, thereby catering to diverse application-specific requirements across various scientific and technological domains. Although the THz chaos demonstrated in this work exhibits low-dimensional characteristics, the results mark a promising initial step in THz QCL chaos study, with potential for performance enhancements and applications. It is noted that in our recent experiments, we observed the chaos generation in another free-running THz QCL emitting at 2.5 THz. Specifically, we measured chaotic bandwidths exceeding 2 GHz (measured at the noise floor) and larger Lyapunov exponents reaching 1.66/ns at 1600 mA, as shown in Fig. S13 (Supplementary Information). These findings indicate that, through further optimization and investigation, free-running THz QCLs may enable the generation of hyper-chaos and support advanced applications that require high-dimensional and complex chaotic signals. Furthermore, similar to the mid-infrared QCL chaos, it is promising to explore the influences of optical feedback and injection[68] on high-dimensional chaos generation in THz QCLs.

Two theoretical models were employed to validate these experimental results and investigate the physical origin of chaos generation in THz QCLs. With the first model, consisting of a full set of effective semiconductor Maxwell-Bloch equations (ESMBEs), we successfully reproduced temporal traces, frequency spectra, and the dynamic scenario as the bias current varied, observed in the experiments. Additionally, the ESMBEs revealed that chaotic behavior is characterized by a broadening of each line in the optical spectrum, as expected. The second model, comprising two coupled complex Ginzburg-Landau equations (CGLEs), features lower mathematical complexity and is thus more suitable for providing insight into the physical origin of chaos in THz QCLs. Using this reduced model, we first demonstrated that an increase in the α factor, which implies stronger phase-amplitude coupling of the electric field, enhances the likelihood of chaotic emission. Furthermore, we observe that a reduction in the total GVD, which can be experimentally controlled using techniques such as chirped mirrors or Gires-Tournois interferometer mirrors, leads to a transition from a comb regime to a chaotic one. This is in accordance with previous studies, which have shown that a decrease in GVD implies a decrease in the slope of the inter-mode phase spectrum[32], corresponding to a loss of locking. These findings provide essential guidelines for designing sources or experimental setups for chaos generation in the THz region. Moreover, this second approach suggests that the physical origin of chaos in free-running THz QCLs might be attributed to the well-known phenomenon of defect-mediated turbulence, typical of extended nonlinear and dissipative systems described by CGLEs.

A systematic exploration of chaotic regimes in THz QCLs presents significant potential, bridging gaps in existing literature and advancing the comprehension of QCL's dynamics. The ability to manipulate and control chaos in the THz region opens unprecedented avenues for innovative technologies with higher performance and versatility. These technologies include broadband spectroscopy, sensing, and free-space communications. Furthermore, chaotic QCLs find applications in LIDAR systems, offering jamming-resistant, high-resolution sensing, or secure multi-channel communications involving chaos modulation for message encryption or synchronized chaos for message transmission. Each mode in multimode chaos possesses the potential to serve as a source for random bit generation. Consequently, the THz QCL chaotic dynamics demonstrated in our study hold significant promise for driving advancements across a variety of technological domains within the THz region.

Methods

THz QCL

The active region of the THz QCL used in this work is based on a hybrid design where bound-to-continuum transitions are exploited for the generation of terahertz photons, while fast longitudinal optical phonon scattering allows the fast depopulation of the lower laser state. The active region is designed for light emission at 4.2 THz. The detailed layer structure of the QCL active region is available in the ref. 69. The entire active region structure was grown by a molecular beam epitaxy system on a semi-insulating GaAs (100) substrate. The grown wafer was then processed into a single plasmon waveguide geometry with a ridge width of 100 μm. To improve the thermal management, the laser substrate was thinned down to 100 μm using grinding and polishing techniques. Various cavity lengths can be made by directly cleaving the laser ridges. The THz QCL used in the experiment has a nominal cavity length of 6 mm and a ridge width of 100 μm.

The continuous wave (cw) output power of the THz QCLs is measured using a THz power meter (Ophir, 3A-P THz), with the lasers operated in constant current mode. To capture THz light emitted from the laser front facet, two parabolic mirrors are employed to collect and focus the light onto a THz power detector. Additionally, the beam path is purged with dry air to reduce water absorption. The emission spectra shown in Fig. S1 are measured with a Fourier transform infrared (FTIR) spectrometer (Bruker, v80) with a spectral resolution of 0.1 cm^{-1} (3 GHz).

Lyapunov exponents

Lyapunov exponents represent the average exponential rates of divergence or convergence of nearby orbits in phase space[43,70]. In a periodic system, the exponents are negative, but in a chaotic system, at least one positive Lyapunov exponent exists. Calculating Lyapunov exponents typically involves three steps: First of all, time delays are computed using the cross-correlation method to determine the dynamic properties of the data. Secondly, the false nearest neighbor method is employed to find an appropriate embedding dimension for effectively representing the data's phase space structure. Finally, by reconstructing the phase space and applying mathematical fitting techniques, Lyapunov exponents are computed to assess the system's chaotic behavior and sensitivity.

Full model based on effective semiconductor Maxwell-Bloch equations

The effective semiconductor Maxwell-Bloch equations (ESMBEs) used in this work describe the multimode dynamics of quantum cascade lasers (QCLs) in the Fabry-Perot (FP) configuration[48]. This model encompasses several fundamental properties of semiconductor materials, including asymmetric gain and refractive index profiles in the frequency domain, a non-zero linewidth enhancement factor, and the dependence of the optical susceptibility on the carrier density. Additionally, the model accounts for spatial hole burning (SHB), manifested as a carrier grating induced by the interference of the counterpropagating fields within the FP resonator. The dynamical variables in the set of ESMBEs are the forward and backward electric fields and polarization terms, the carrier density, and the carrier grating. The ESMBE parameters used in the simulations are listed in Table S1, Supplementary Information.

Reduced model based on complex Ginzburg-Landau equations

The reduced model is based on two coupled complex Ginzburg-Landau equations (CGLEs), Eqs. (1), (2), derived from the full ESMBE model under the assumption of fast carriers and near-threshold operation[18,53], using an approach analogous to that recently employed to describe Kerr solitons in driven and passive microresonators[71]. This model describes the multimode dynamics of QCLs in the Fabry-Perot (FP) configuration. The dynamical variables of the two CGLEs are the forward and backward counterpropagating fields inside the FP cavity. The coupling between these fields is due to spatial hole burning (SHB), which is included in the model. Additionally, the CGLEs account for a non-zero linewidth enhancement factor and group velocity dispersion. The parameters used in the simulations with the reduced model are listed in Table S2, Supplementary Information. In order to estimate the material GVD, we rearrange Eq. (1), obtaining:

$$\begin{aligned}\frac{\partial F^+}{\partial \eta}+\frac{\partial F^+}{\partial t} &= -F^+ + (1+i\alpha)\mu F^+ - (1+i\alpha)2(|F^+|^2+2|F^-|^2)F^+ \\ &\quad + \left(\frac{\sigma^2}{\Gamma^2(1+\alpha^2)} + i\frac{v_g}{2\tau_p}\left(k'' - \frac{2\tau_p\alpha\sigma^2}{v_g\Gamma^2(1+\alpha^2)}\right)\right)\frac{\partial^2 F^+}{\partial \eta^2}\end{aligned} \tag{3}$$

We define the total group velocity dispersion as:

$$\mathrm{GVD}_{\mathrm{tot}} = k'' - \frac{2\tau_p\alpha\sigma^2}{v_g\Gamma^2(1+\alpha^2)} \tag{4}$$

Therefore, we observe that $\mathrm{GVD}_{\mathrm{tot}}$ is expressed as the sum of k'' (waveguide GVD) and the material GVD given by:

$$\mathrm{GVD}_{\mathrm{mat}} = -\frac{2\tau_p\alpha\sigma^2}{v_g\Gamma^2(1+\alpha^2)} \tag{5}$$

We highlight the diffusive and dispersive role of the differential term on the right-hand side of Eq. (3). We can estimate $\mathrm{GVD}_{\mathrm{mat}}$ by using the parameters exploited in the numerical simulations (see Table S2), obtaining $\mathrm{GVD}_{\mathrm{mat}} = -77{,}024\ \mathrm{fs}^2/\mathrm{mm}$.

Data availability

The data that support the findings of this study are available from the corresponding author upon request.

Code availability

The algorithms and datasets used to the numerical integration of the reduced model consisting in Eqs. (1)-(2) in the paper are freely available at this link: https://www.dropbox.com/scl/fo/3ukh74gtds0rbgnmf68tk/AExsopGaWUeIjcCS1Tq7grA?rlkey=p29kc6ghjg1cxoulia41sb1k6&st=muadr8oc&dl=0. The algorithms used to integrate the ESMBEs were also developed by authors who are not included in the authorship of this work. Thus, they cannot be made immediately available, but the corresponding author will consider reasonable requests and consult the code authors accordingly.

References

1. Lorenz, E. N. Deterministic nonperiodic flow. *J. Atmos. Sci.* **20**, 130–141 (1963).
2. Haken, H. Analogy between higher instabilities in fluids and lasers. *Phys. Lett. A* **53**, 77–78 (1975).
3. Weiss, C. O., Abraham, N. B. & Hübner, U. Homoclinic and heteroclinic chaos in a single-mode laser. *Phys. Rev. Lett.* **61**, 1587–1590 (1988).
4. Bracikowski, C. & Roy, R. Chaos in a multimode solid-state laser system. *Chaos: Interdiscip. J. Nonlinear Sci.* **1**, 49–64 (1991).
5. VanWiggeren, G. D. & Roy, R. Communication with chaotic lasers. *Science* **279**, 1198–1200 (1998).
6. Deng, Y. et al. Mid-infrared hyperchaos of interband cascade lasers. *Light Sci. Appl.* **11**, 7 (2022).
7. Arecchi, F., Lippi, G., Puccioni, G. & Tredicce, J. Deterministic chaos in laser with injected signal. *Opt. Commun.* **51**, 308–314 (1984).
8. Virte, M., Panajotov, K., Thienpont, H. & Sciamanna, M. Deterministic polarization chaos from a laser diode. *Nat. Photonics* **7**, 61–65 (2013).
9. Sciamanna, M. & Shore, K. A. Physics and applications of laser diode chaos. *Nat. Photonics* **9**, 151–162 (2015).
10. Ohtsubo, J. *Semiconductor Lasers: Stability, Instability and Chaos* (Springer International Publishing, 2017).
11. Simpson, T., Liu, J., Gavrielides, A., Kovanis, V. & Alsing, P. Period-doubling route to chaos in a semiconductor laser subject to optical injection. *Appl. Phys. Lett.* **64**, 3539–3541 (1994).
12. Kreinberg, S. et al. Mutual coupling and synchronization of optically coupled quantum-dot micropillar lasers at ultra-low light levels. *Nat. Commun.* **10**, 1539 (2019).
13. Maruskin, J. *Bifurcations and Chaos*. (De Gruyter, Berlin, Boston, 2018).
14. Mukai, T. & Otsuka, K. New route to optical chaos: Successive-subharmonic-oscil- lation cascade in a semiconductor laser coupled to an external cavity. *Phys. Rev. Lett.* **55**, 1711–1714 (1985).
15. Wieczorek, S., Krauskopf, B., Simpson, T. & Lenstra, D. The dynamical complexity of optically injected semiconductor lasers. *Phys. Rep.* **416**, 1–128 (2005).
16. Tang, S. & Liu, J. Chaotic pulsing and quasi-periodic route to chaos in a semiconductor laser with delayed opto-electronic feedback. *IEEE J. Quantum Electron.* **37**, 329–336 (2001).
17. Viktorov, E. A. et al. Stability of the mode-locked regime in quantum dot lasers. *Appl. Phys. Lett.* **91**, 231116 (2007).
18. Columbo, L. et al. Unifying frequency combs in active and passive cavities: Temporal solitons in externally driven ring lasers. *Phys. Rev. Lett.* **126**, 173903 (2021).

19. Gordon, A. et al. Multimode regimes in quantum cascade lasers: From coherent instabilities to spatial hole burning. *Phys. Rev. A-At., Mol., Opt. Phys.* **77**, 053804 (2008).
20. Li, J.-C., Xiao, J.-L., Yang, Y.-D., Chen, Y.-L. & Huang, Y.-Z. Random bit generation based on a self-chaotic microlaser with enhanced chaotic bandwidth. *Nanophotonics* **12**, 4109–4116 (2023).
21. Spitz, O. et al. Private communication with quantum cascade laser photonic chaos. *Nat. Commun.* **12**, 3327 (2021).
22. Uchida, A. et al. Fast physical random bit generation with chaotic semiconductor lasers. *Nat. Photonics* **2**, 728–732 (2008).
23. Chen, R. et al. Breaking the temporal and frequency congestion of lidar by parallel chaos. *Nat. Photonics* **17**, 306–314 (2023).
24. Kanter, I., Aviad, Y., Reidler, I., Cohen, E. & Rosenbluh, M. An optical ultrafast random bit generator. *Nat. Photonics* **4**, 58–61 (2010).
25. Yoshimura, K. et al. Secure key distribution using correlated randomness in lasers driven by common random light. *Phys. Rev. Lett.* **108**, 070602 (2012).
26. Gulevich, D., Koshelets, V. & Kusmartsev, F. Bridging the terahertz gap for chaotic sources with superconducting junctions. *Phys. Rev. B* **99**, 060501 (2019).
27. Kuwashima, F. et al. Highly efficient THz waves using laser chaos. In *2023 48th International Conference on Infrared, Millimeter, and Terahertz Waves (IRMMW-THz)*, 1–2 (IEEE, 2023).
28. Kuwashima, F. et al. Stability of optical beats in laser chaos for THz wave generation and detection. In *2021 46th International Conference on Infrared, Millimeter and Terahertz Waves (IRMMW-THz)*, 1–2 (IEEE, 2021).
29. Faist, J. et al. Quantum cascade laser. *Science* **264**, 553–556 (1994).
30. Köhler, R. et al. Terahertz semiconductor-heterostructure laser. *Nature* **417**, 156–159 (2002).
31. Heckelmann, I. et al. Quantum walk comb in a fast gain laser. *Science* **382**, 434–438 (2023).
32. Opačak, N. & Schwarz, B. Theory of frequency-modulated combs in lasers with spatial hole burning, dispersion, and Kerr nonlinearity. *Phys. Rev. Lett.* **123**, 243902 (2019).
33. Jumpertz, L., Schires, K., Carras, M., Sciamanna, M. & Grillot, F. Chaotic light at mid-infrared wavelength. *Light Sci. Appl.* **5**, e16088 (2016).
34. Spitz, O., Wu, J., Carras, M., Wong, C.-W. & Grillot, F. Chaotic optical power dropouts driven by low frequency bias forcing in a mid-infrared quantum cascade laser. *Sci. Rep.* **9**, 4451 (2019).
35. Derntl, C. G. et al. Gain dynamics in a heterogeneous terahertz quantum cascade laser. *Appl. Phys. Lett.* **113**, 181102 (2018).
36. Piccardo, M. & Capasso, F. Laser frequency combs with fast gain recovery: Physics and applications. *Laser Photonics Rev.* **16**, 2100403 (2022).
37. Piccardo, M. et al. Frequency-modulated combs obey a variational principle. *Phys. Rev. Lett.* **122**, 253901 (2019).
38. Li, H. et al. Dynamics of ultra-broadband terahertz quantum cascade lasers for comb operation. *Opt. Express* **23**, 33270–33294 (2015).
39. Li, H. et al. Real-time multimode dynamics of terahertz quantum cascade lasers via intracavity self-detection: observation of self-mode-locked population pulsations. *Opt. Express* **30**, 3215–3229 (2022).
40. Rösch, M., Scalari, G., Beck, M. & Faist, J. Octave-spanning semiconductor laser. *Nat. Photonics* **9**, 42–47 (2015).
41. Garrasi, K. et al. High dynamic range, heterogeneous, terahertz quantum cascade lasers featuring thermally tunable frequency comb operation over a broad current range. *ACS Photonics* **6**, 73–78 (2018).
42. Renjini, A., Raj, V., Swapna, M., Sreejyothi, S. & Sankararaman, S. Phase portrait for high fidelity feature extraction and classification: A surrogate approach. *Chaos: Interdiscip. J. Nonlinear Sci.* **30**, 113122 (2020).
43. Wolf, A., Swift, J. B., Swinney, H. L. & Vastano, J. A. Determining Lyapunov exponents from a time series. *Phys. D: Nonlinear Phenom.* **16**, 285–317 (1985).
44. Grassberger, P. & Procaccia, I. Characterization of strange attractors. *Phys. Rev. Lett.* **50**, 346 (1983).
45. Kang, H. et al. Observation of optical chaotic solitons and modulated subharmonic route to chaos in mode-locked laser. *Phys. Rev. Lett.* **133**, 263801 (2024).
46. Prati, F. & Columbo, L. Long-wavelength instability in broad-area semiconductor lasers. *Phys. Rev. A* **75**, 053811 (2007).
47. Columbo, L. L., Barbieri, S., Sirtori, C. & Brambilla, M. Dynamics of a broad-band quantum cascade laser: from chaos to coherent dynamics and mode-locking. *Opt. Express* **26**, 2829–2847 (2018).
48. Silvestri, C., Columbo, L. L., Brambilla, M. & Gioannini, M. Coherent multi-mode dynamics in a quantum cascade laser: amplitude-and frequency-modulated optical frequency combs. *Opt. Express* **28**, 23846–23861 (2020).
49. Silvestri, C., Qi, X., Taimre, T. & Rakić, A. D. Multimode dynamics of terahertz quantum cascade lasers: Spontaneous and actively induced generation of dense and harmonic coherent regimes. *Phys. Rev. A* **106**, 053526 (2022).
50. Taimre, T. et al. Laser feedback interferometry: a tutorial on the self-mixing effect for coherent sensing. *Adv. Opt. Photonics* **7**, 570–631 (2015).
51. Kane, D. M. & Shore, K. A. *Unlocking dynamical diversity: optical feedback effects on semiconductor lasers* (John Wiley & Sons, 2005).
52. Dente, G. C., Durkin, P. S., Wilson, K. A. & Moeller, C. E. Chaos in the coherence collapse of semiconductor lasers. *IEEE J. Quantum Electron.* **24**, 2441–2447 (1988).
53. Silvestri, C., Brambilla, M., Bardella, P. & Columbo, L. L. Unified theory for frequency combs in ring and Fabry-perot quantum cascade lasers: An order-parameter equation approach. *APL Photonics* **9**, 076119 (2024).
54. Silvestri, C., Qi, X., Taimre, T., Bertling, K. & Rakić, A. D. Frequency combs in quantum cascade lasers: An overview of modeling and experiments. *APL Photonics* **8**, 020902 (2023).
55. Piccardo, M. et al. Frequency combs induced by phase turbulence. *Nature* **582**, 360–364 (2020).
56. Jumpertz, L. et al. Measurements of the linewidth enhancement factor of mid-infrared quantum cascade lasers by different optical feedback techniques. *AIP Adv.* **6**, 015212 (2016).
57. Bachmann, D. et al. Dispersion in a broadband terahertz quantum cascade laser. *Appl. Phys. Lett.* **109**, 221107 (2016).
58. Burghoff, D. et al. Terahertz laser frequency combs. *Nat. Photonics* **8**, 462–467 (2014).
59. Villares, G. et al. Dispersion engineering of quantum cascade laser frequency combs. *Optica* **3**, 252–258 (2016).
60. Hillbrand, J., Jouy, P., Beck, M. & Faist, J. Tunable dispersion compensation of quantum cascade laser frequency combs. *Opt. Lett.* **43**, 1746–1749 (2018).
61. Lu, Q. Y., Manna, S., Wu, D. H., Slivken, S. & Razeghi, M. Shortwave quantum cascade laser frequency comb for multi-heterodyne spectroscopy. *Appl. Phys. Lett.* **112**, 141104 (2018).
62. Wang, F. et al. Short terahertz pulse generation from a dispersion compensated modelocked semiconductor laser. *Laser Photonics Rev.* **11**, 1700013 (2017).
63. Aranson, I. S. & Kramer, L. The world of the complex Ginzburg-Landau equation. *Rev. Mod. Phys.* **74**, 99–143 (2002).
64. Opačak, N. et al. Nozaki–Bekki solitons in semiconductor lasers. *Nature* **625**, 685–690 (2024).
65. Chate, H. Spatiotemporal intermittency regimes of the one-dimensional complex Ginzburg-Landau equation. *Nonlinearity* **7**, 185 (1994).

66. Spitz, O. & Grillot, F. A review of recent results of mid-infrared quantum cascade photonic devices operating under external optical control. *J. Phys.: Photonics* **4**, 022001 (2022).
67. Spitz, O. et al. Investigation of chaotic and spiking dynamics in mid-infrared quantum cascade lasers operating continuous-waves and under current modulation. *IEEE J. Sel. Top. Quantum Electron.* **25**, 1200311 (2019).
68. Vicente, R., Dauden, J., Colet, P. & Toral, R. Analysis and characterization of the hyperchaos generated by a semiconductor laser subject to a delayed feedback loop. *IEEE J. Quantum Electron.* **41**, 541–548 (2005).
69. Wan, W., Li, H., Zhou, T. & Cao, J. Homogeneous spectral spanning of terahertz semiconductor lasers with radio frequency modulation. *Sci. Rep.* **7**, 44109 (2017).
70. Sprott, J. C. *Chaos and time-series analysis* (Oxford University Press, 2003).
71. Cole, D. C., Gatti, A., Papp, S. B., Prati, F. & Lugiato, L. Theory of Kerr frequency combs in Fabry-Perot resonators. *Phys. Rev. A* **98**, 013831 (2018).

Acknowledgements

This work is supported by the National Science Fund for Distinguished Young Scholars (62325509), the Innovation Program for Quantum Science and Technology (2023ZD0301000), the National Natural Science Foundation of China (62235019, 61875220, 61927813, 61991430, 62035005, 62105351, 62275258, 62035014 and 62305364), Science and Technology Commission of Shanghai Municipality (21ZR1474600), the "From 0 to 1" Innovation Program of the Chinese Academy of Sciences (ZDBS-LY-JSC009), and the CAS Project for Young Scientists in Basic Research (YSBR-069). M.B. and L.C. acknowledge the research funding from the Italian Ministerial PRIN project "MIRABILIS" (CUPM. D53D23002780006).

Author contributions

B.L., C.S., and K.Z. contributed equally to this work. H.L. conceived the study. Z.L., X.M., B.L., and W.W. fabricated the THz QCLs. B.L., K.Z., X.M., S.W., and H.L. performed experimental measurements. C.S., M.B., and L.L.C. carried out numerical simulations based on the full model and reduced model. Y.Z., J.P., and H.Z. performed the analysis of the Lyapunov exponents of the THz QCL. H.L., L.L.C., B.L., C.S., K.Z., J.P., H.Z., C.W., and Z.Z. participated in the data analysis. B.L., H.L, C.S., L.L.C., and K.Z. wrote the manuscript with contributions from all authors. H.L., L.L.C., and H.Z. supervised the project.

Competing interests

The authors declare no competing interests.

Additional information

Supplementary information The online version contains supplementary material available at https://doi.org/10.1038/s41467-025-64921-x.

Correspondence and requests for materials should be addressed to Heping Zeng, Lorenzo Luigi Columbo or Hua Li.

Peer review information *Nature Communications* thanks Kathy Lüdge and the other anonymous reviewer(s) for their contribution to the peer review of this work. A peer review file is available.

Reprints and permissions information is available at http://www.nature.com/reprints